ACS Photonics

Article

pubs.acs.org/journal/apchd5

Waveguide Scattering Microscopy for Dark-Field Imaging and Spectroscopy of Photonic Nanostructures

David J. Hill, Christopher W. Pinion, Joseph D. Christesen, and James F. Cahoon*

Department of Chemistry, University of North Carolina at Chapel Hill, Chapel Hill, North Carolina 27599-3290, United States

Ⓢ *Supporting Information*

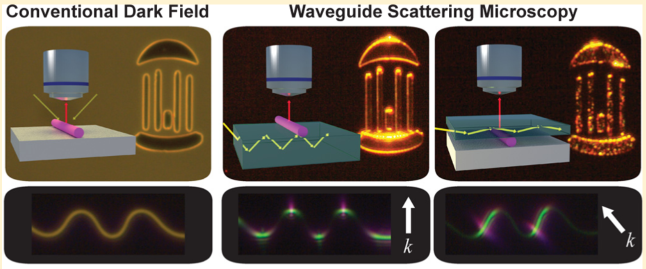

ABSTRACT: Dark-field microscopy (DFM) is widely used to optically image and spectroscopically analyze nanoscale objects. In a typical DFM configuration, a sample is illuminated at oblique angles and an objective lens collects light scattered by the sample at a range of lower angles. Here, we develop waveguide scattering microscopy (WSM) as an alternative technique to image and analyze photonic nanostructures. WSM uses an incoherent white-light source coupled to a dielectric slab waveguide to generate an evanescent field that illuminates objects located within several hundred nanometers of the waveguide surface. Using standard microscope slides or coverslips as the waveguide, we demonstrate high-contrast dark-field imaging of nanophotonic and plasmonic structures such as Si nanowires, Au nanorods, and Ag nanoholes. Scattering spectra collected in the WSM configuration show excellent signal-to-noise with minimal background signal compared to conventional DFM. In addition, the polarization of the incident field is controlled by the direction of the propagating wave, providing a straightforward route to excite specific optical modes in anisotropic nanostructures by selecting the appropriate input wavevector. Considering the facile integration of WSM with standard microscopy equipment, we anticipate it will become a versatile tool for characterizing photonic nanostructures.

KEYWORDS: *dark-field microscopy, waveguide scattering microscopy, total internal reflection microscopy, plasmonics, nanophotonics*

Dark-field microscopy (DFM) is used extensively in biological and materials research for applications ranging from single nanoparticle spectroscopy[1−7] to label-free live tissue imaging.[3,8−13] As illustrated in Figure 1A, DFM typically requires white-light illumination of a sample at oblique angles and collection of the scattered light by an objective lens, producing a bright object surrounded by a dark background. In nanomaterials research, DFM has become particularly useful because nanoscale objects strongly scatter light at specific wavelengths as a result of optical resonances that depend on the size, shape, and composition of the material. For instance, Mie resonances in semiconductor nanowires (NWs) produce distinct colors that strongly depend on the wire diameter,[14−17] and the frequencies of localized surface plasmon resonances in anisotropic metallic nanoparticles are well known to depend on the particle size and aspect ratio.[1−7,18] When integrated with a spectrometer, DFM enables quantitative measurement of these types of wavelength-dependent scattering characteristics in single nanoscale objects.

Despite the ubiquity of DFM, the technique presents several limitations or caveats. First, the angular distribution of the white-light source varies from microscope to microscope, producing a range of results from the same sample when imaged with different DFM systems.[19,20] Second, the polarization of the input white light is difficult to control because of the angular distribution of the incoming rays, preventing highly selective excitation of polarization-dependent optical resonances in anisotropic objects.[21] Third, the incident light is supplied by a lens, which limits the range of angles that can be collected by the objective lens and reduces the numerical aperture and resolution of the image.

Here, we describe an alternative DFM method called waveguide scattering microscopy (WSM),[22−24] which illuminates nanoscale objects in the near field using white light transmitted through a multimode dielectric slab waveguide. Light scattered into the far field is collected by an objective lens to generate a dark-field, full-color image. WSM is similar to both total internal reflection microscopy (TIRM)[25−30] and total internal reflection fluorescence microscopy (TIRFM),[31,32] but it uses an incoherent white-light source coupled to a waveguide to generate the evanescent field rather than a laser source coupled to a lens or prism. In a few instances, TIRM has been performed with white-light illumination to evaluate plasmon resonances in Au nanoparticles.[25−28] Similarly, Au nanorods have been deposited and imaged on the surface of an optical fiber waveguide coupled to a halogen lamp.[33] Waveguide-based variations of TIRFM have also been performed by coupling laser or diode light sources into glass waveguides.[34−39] In addition, optical fiber waveguides and slab waveguides are commonly used to perform spectroscopy in both the infrared[5] and optical[6] regimes on samples deposited in the near field of

Received: May 9, 2014
Published: July 15, 2014

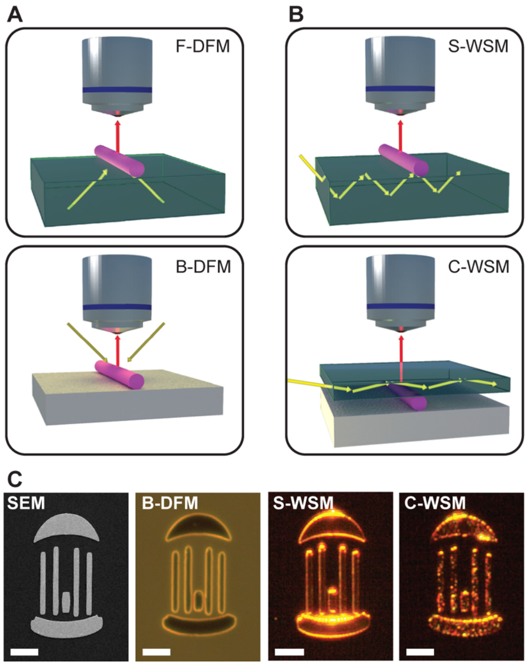

Figure 1. Comparison of conventional DFM and WSM. (A) Schematic of conventional forward-scattering (upper) and backward-scattering (lower) DFM systems. (B) Schematic of a substrate-based (upper) and coverslip-based (lower) WSM apparatus. Green substrates indicate transparent materials, and white substrates indicate opaque materials; however, the substrate in B-DFM and C-WSM may be opaque or transparent. In C-WSM, an index-matching oil is placed in the vicinity of the nanostructure to enhance optical coupling. (C) Images of a micropatterned logo defined in a 50 nm thick Au film by electron-beam lithography on glass, showing SEM image (far left) and DFM (middle left), S-WSM (middle right), and C-WSM (far right) optical images with a 10× microscope objective; all scale bars, 20 μm.

the waveguide surface. Here, we use WSM to both image and spectroscopically analyze plasmonic and photonic nanostructures. It is used to produce images and spectra with high signal-to-background ratios and to excite polarization-dependent scattering modes in metallic and dielectric nanostructures. WSM is surprisingly easy to implement using standard microscope equipment and can overcome limitations encountered with standard DFM for specific applications.

■ RESULTS AND DISCUSSION

A standard DFM configuration is illustrated schematically in Figure 1A for both forward-scattering (F-DFM) and backward-scattering (B-DFM) geometries. In F-DFM, the substrate is transparent and light is incident and collected on opposite sides of the substrate. In B-DFM, the substrate is often opaque and light is incident and collected on one side. Two analogous WSM configurations are illustrated in Figure 1B. If the substrate is transparent (such as a standard glass microscopy slide), then total internal reflection of white light within the substrate provides waveguide illumination for objects on the surface. If the substrate is opaque, a coverslip can be placed on the substrate using an optical-quality oil at the interface between the nanostructure and coverslip. Total internal reflection within the coverslip provides waveguide illumination, and the oil serves to improve light coupling by homogenizing the local refractive index and increasing physical contact between the substrate and coverslip through capillary forces. In the two WSM configurations, referred to as substrate waveguide scattering microscopy (S-WSM) and coverslip waveguide scattering microscopy (C-WSM), respectively, light scattered out of the waveguide by the sample is collected with an objective lens to form a dark-field image.

We implemented WSM on a standard upright microscope (Zeiss Axio Imager A2M; see Figure S1) using an inexpensive fiber-coupled tungsten halogen lamp as the white-light source. The white light was coupled into standard microscope slides and coverslips at the unpolished edges of the glass (see Figure S2 and Methods). A comparison of dark-field images generated with B-DFM, S-WSM, and C-WSM is shown in Figure 1C for a simple micron-scale Au pattern deposited on a glass substrate. The B-DFM produces an image with significant background signal due to refraction and reflection within the substrate. In contrast, the two WSM modes produce high-contrast images with negligible background signal. In addition, the S-WSM exhibits sensitivity to the edges of the pattern, whereas C-WSM is sensitive to surface topology, producing an image of surface irregularities in the Au film. This latter effect results from the high surface sensitivity of the evanescent field (see Figure S3) combined with the positioning of the waveguide between nanostructure and objective.

In addition to imaging, DFM is extensively used for the spectroscopic analysis of nanostructures, such as Au nanoparticles and nanorods exhibiting localized surface plasmon resonances.[2,7,18,40,41] Similar to previous analyses of Au nanostructures by TIRM[25−28] and optical fibers,[33] WSM can be used to image and analyze these materials, as illustrated in Figure 2. Au nanorods ~150 × 50 nm in length and diameter, respectively (Figure 2A), appear as bright orange spots in both B-DFM and S-WSM (Figure 2B). S-WSM provides an image with substantially improved contrast ratio because of the suppressed background scattering. Optical simulations of the plasmon resonance in these particles using finite-difference frequency-domain (FDFD) calculations (see Methods) demonstrate that the optical field in both DFM and WSM (Figure 2C and D, respectively, as well as Figure S4) can excite the transverse and longitudinal plasmon resonances in the nanorod.

Scattering signals, as shown in Figure 2E, were measured from the same ensemble of nanorods using B-DFM and S-WSM. Background signals (without nanorods) were also measured and subtracted from the scattering signals to yield the final scattering spectra, as shown in Figure 2F. Although background subtraction is critically important for DFM, the background signal from WSM is both low in amplitude and spectrally featureless (e.g., compare red and blue dashed curves in Figure 2E), eliminating the need to collect a background spectrum. Quantitatively, the maximum signal-to-background ratio for DFM is ~2.2, whereas the maximum value for WSM is ~14 000. Background suppression is thus one key advantage of WSM over DFM for the spectroscopic analysis of photonic nanostructures. As expected from the optical simulations, the DFM and WSM spectra both exhibit peaks for the longitudinal (~670 nm) and transverse (~550 nm) modes.

We also investigated the scattering spectra from Si NWs, which behave as cylindrical, subwavelength Mie scattering centers.[14−17] Because the wires lie on substrates that break the cylindrical symmetry, scattering peaks measured by DFM tend to shift with the various illumination angles produced by different microscope objectives. This type of substrate effect has been observed in the scattering from plasmonic nanoparticles.[42] In some cases, it can be used advantageously to excite specific,

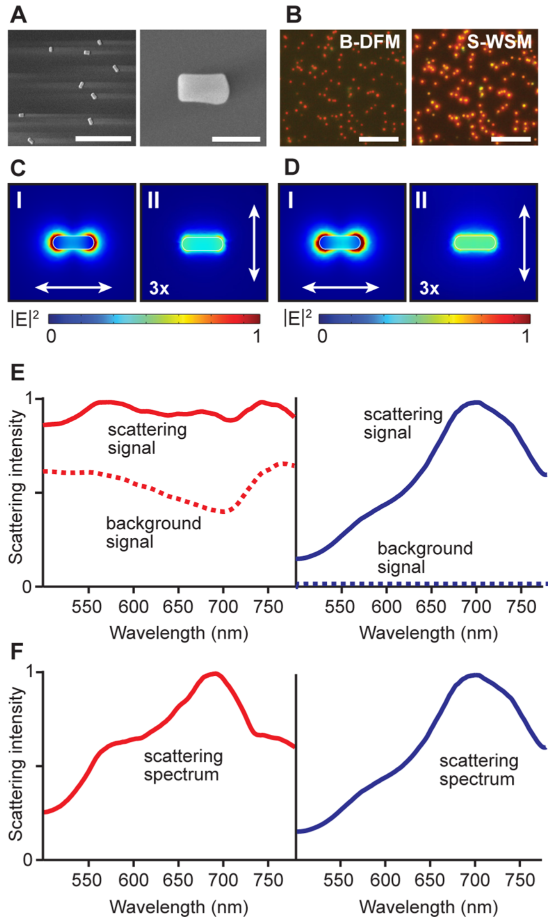

Figure 2. Comparison of scattering spectra from plasmonic nanorods acquired with DFM and WSM. (A) SEM images of Au nanorods; scale bars, 1 μm (left) and 100 nm (right). (B) B-DFM image (left) and S-WSM image (right) of multiple Au nanorods; scale bars, 50 μm. (C and D) Optical simulations of the longitudinal (I) and transverse (II) plasmon resonances in Au nanorods on a glass substrate excited using a plane wave incident at 60° with respect to the surface normal (panel C) or waveguided in the substrate (panel D), representing DFM and S-WSM configurations, respectively. Directions of the electric field polarizations are denoted by double-headed arrows, and intensities of the transverse modes (II) are scaled by a factor of 3 to increase their visibility. See Figure S4 for cross-sectional images of these resonances. (E) Scattering signal collected from an ensemble of Au nanorods (solid) and background signal (dashed) collected from the substrate for B-DFM (left, red) and S-WSM (right, blue). (F) Scattering spectrum of Au nanorods generated by subtracting the substrate background signal from the scattering signal in panel E for B-DFM (left) and S-WSM (right). Differences in the scattering spectrum result from differences in the illumination geometry, which shift the relative intensities and resonance frequencies of individual nanorods. All spectra in panels E and F were corrected based on the spectrum of the white-light sources (see Methods).

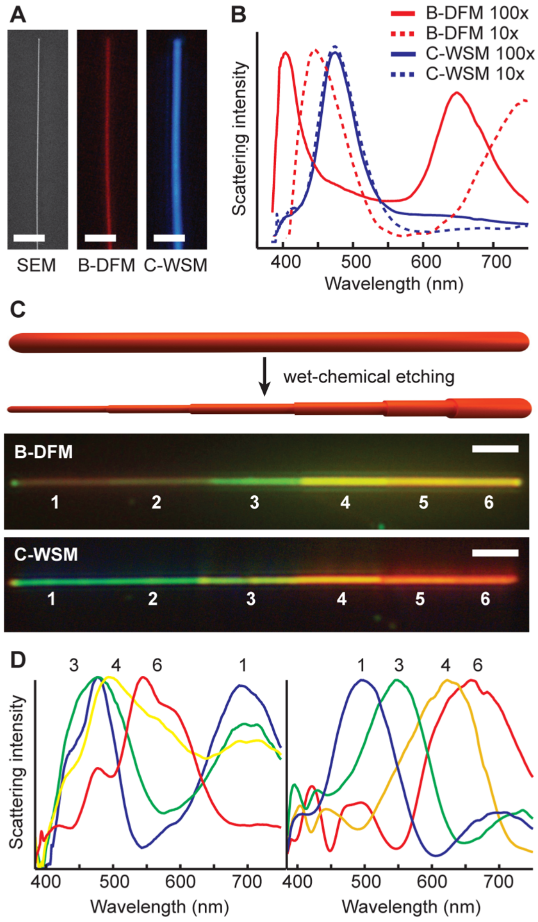

Figure 3. Comparison of Mie scattering spectra from Si NWs acquired with DFM and WSM. (A) SEM (left), DFM (middle), and WSM (right) images of a 50 nm diameter Si NW; scale bars, 2 μm. (B) Comparison of the scattering spectra using DFM with a 100× objective (solid red) and 10× objective (dashed red) and C-WSM with a 100× objective (solid blue) and 10× objective (dashed blue). (C) Upper: Schematic illustration of a Si NW encoded with six distinct diameters by the ENGRAVE process, which uses selective wet-chemical etching to reduce the wire diameter. Lower: Images collected by B-DFM (top) and C-WSM (bottom) of the diameter-encoded NW; scale bars, 5 μm. Regions of different diameter are denoted by the numbers 1−6. (D) Scattering spectra collected by B-DFM (left) and C-WSM (right) of select regions of the NW shown in panel C.

angle-dependent optical resonances, although it also adds a complication to the interpretation of scattering spectra. This effect is illustrated by DFM and WSM images and scattering spectra (Figure 3A and B, respectively) collected on the same Si NW 50 nm in diameter. A conventional DFM image collected with a 100× objective shows a red NW, and scattering spectra (red curve) show Mie resonances at ~405 and ~650 nm. For DFM collected with a 10× objective (red dashed curve in Figure 3B), however, the Mie resonances red shift by ~40 and ~100 nm for the short- and long-wavelength peaks, respectively. In contrast, WSM produces images with a blue color and spectra that show a single Mie scattering resonance (blue curves in Figure 3B). Most importantly, the scattering resonance observed with WSM does not shift with the microscope objective, showing a peak at ~470 nm with both 100× and 10× objectives.

To examine the diameter-dependent scattering of Si NWs, we fabricated a single NW with six distinct diameters along the growth axis (Figure 3C) using the ENGRAVE (Encoded Nanowire GRowth and Appearance through VLS and Etching) process described elsewhere.[43] For the largest diameters (~200 nm), the wire scatters yellow or red light followed by progressively shorter wavelengths for smaller diameters, producing the rainbow effect in the images in Figure 3C. C-WSM scattering spectra collected from sections with distinct diameters (Figure 3D, right) confirm a smooth shift of the scattering peaks to shorter wavelengths. For B-DFM, however, the spectral response (Figure 3D, left) is more complex because of the broad distribution of input wavevectors, and a clear progression is not easily discerned.

In addition to diameter-dependent effects, the scattering of anisotropic nanostructures depends on the polarization of the electromagnetic field. In DFM, polarization control is exerted by placing polarization optics in the incident or scattered beam paths. In WSM, however, polarization control can be achieved simply by changing the direction of the wavevector, *k*, for the light source (see Figure S5 for details). Light in a multimode waveguide is composed of both s-polarized and p-polarized fields, as illustrated in Figure 4A.[44] At the waveguide surface, however, the evanescent field is linearly polarized (parallel to the surface) for the s-polarized light and is elliptically polarized in the plane of incidence for the p-polarized light (with components primarily perpendicular but also parallel to the surface).[26,27,45] For nanostructures with high aspect ratios, particularly NWs,[46] light scattering is strongly favored for light polarized parallel to the long axis of the structure. For nanostructures lying on the waveguide surface, this results in preferential scattering by s-polarized light if the long axis of the nanostructure is oriented perpendicular to *k*, referred to as the transverse magnetic (TM) direction (Figure 4A top). Orientation parallel to *k*, referred to as the transverse electric (TE) direction, minimizes scattering by the s-polarization (Figure 4A bottom). Because anisotropic structures are typically oriented with the long axis parallel to the substrate surface, scattering from p-polarized light is minimal (see Figure S6).

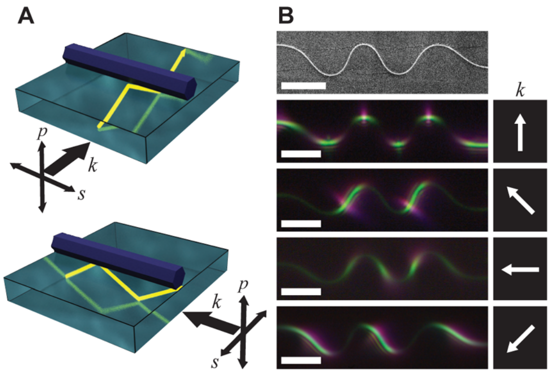

Figure 4. Polarization-selective illumination of Si NWs with WSM. (A) Schematic of TM (top) and TE (bottom) waveguide illumination of a NW, showing the s-polarized electric field parallel and perpendicular, respectively, to the wire axis. (B) SEM (top) and WSM images (bottom) of a sinusoidal Si NW under waveguide illumination using the wavevector directions denoted by arrows; scale bars, 5 μm.

This polarization effect is well illustrated by WSM images collected on a sinusoidal Si NW using four distinct directions for *k* (Figure 4B), achieved by altering the position of the light source relative to the nanowire axis (see Figure S5). Sinusoidal wires were created following a literature procedure[47] for depositing NWs on a flexible, stretched polydimethylsiloxane (PDMS) substrate, which was then released to form bent wires in a planar sinusoidal shape (see Methods for details). Because PDMS is transparent, it was also utilized as the waveguide substrate, illustrating the generality of the WSM technique for any planar, optically transparent substrate material. As shown by the WSM images for specific *k* directions in Figure 4B, segments of the wire satisfying the TM condition exhibit strong light scattering, whereas segments satisfying the TE condition are dark. These images confirm that light scattering primarily results from the s-polarization and confirm that the input *k* direction provides polarization control for imaging and analysis of anisotropic nanostructures by WSM.

To demonstrate WSM polarization control with plasmonic nanostructures, we fabricated an asymmetric array of rectangular nanoholes in an Ag film deposited on a glass substrate, as shown in Figure 5A (see Methods for fabrication details). Plasmon resonances in these types of structures have been shown to depend on the polarization of incoming light, causing the transmission of different wavelengths for orthogonal polarizations of the incoming beam.[48−50] As shown in Figure 5B, we performed optical simulations of the Ag nanohole array under waveguide illumination with the wavevector parallel (vertical s-polarization) and perpendicular (horizontal s-polarization) to the long axis of the array. These simulations confirm that distinct surface plasmon resonances can be excited by the waveguide at wavelengths of ∼600 nm for the vertical polarization and ∼800 nm for the horizontal polarization.

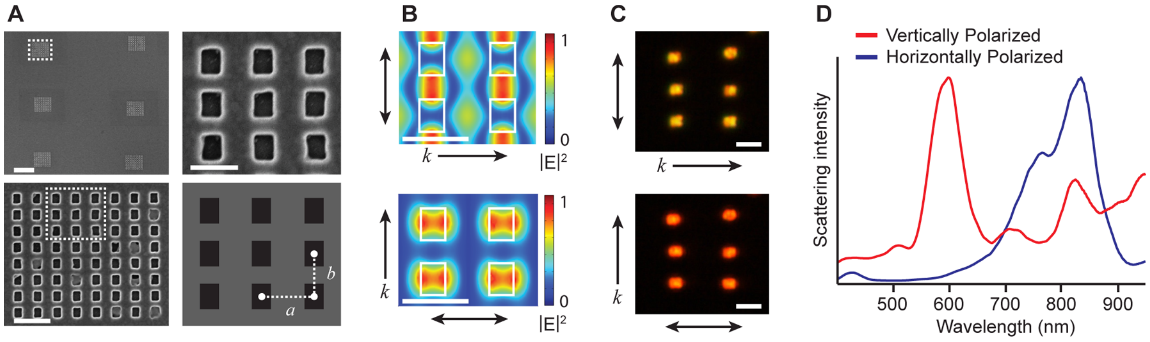

Figure 5. Polarization-selective illumination of plasmonic Ag nanohole arrays with WSM. (A) SEM images of a set of six 8 × 8 Ag nanohole arrays, showing all six arrays (upper left; scale bar, 5 μm), a magnified image of a single 8 × 8 array (lower left; scale bar, 1 μm), and a magnified image of nine nanoholes (upper right; scale bar, 500 nm). Dashed white boxes denote the magnified regions. Lower right: Nanohole geometry used for optical simulations with a horizontal pitch, *a*, of 550 nm and vertical pitch, *b*, of 450 nm (B) FDFD optical simulations showing the electric field intensity ($|E|^2$) 40 nm above the surface of the Ag film for vertically (upper) and horizontally (lower) s-polarized illumination of the array with wavevector and polarization directions indicated by single- and double-headed arrows, respectively; scale bars, 500 nm. (C) WSM images of six 8 × 8 nanohole arrays obtained for vertically (upper) and horizontally (lower) s-polarized illumination; scale bar, 1 μm. (D) WSM scattering spectra obtained for vertically (red) and horizontally (blue) s-polarized illumination of the nanohole arrays shown in panel C.

WSM images of the nanohole arrays show two distinct colors from the horizontal and vertical polarization conditions (Figure 5C). Scattering spectra collected in these two conditions (Figure 5D) show distinct scattering resonances located at ~600 nm for the vertical polarization and 750−850 nm for the horizontal polarization. This result confirms that the direction of the input wavevector, *k*, in WSM can be used to produce polarization-resolved imaging and scattering spectra from anisotropic plasmonic nanostructures. Furthermore, it highlights the similarity of the data produced by WSM—without polarization optics—to the data collected with more conventional polarization optics.[48−50]

■ CONCLUSIONS

Conventional DFM has proven to be a valuable tool for the study of plasmonic and photonic nanostructures. WSM represents a complementary dark-field technique that can have advantages over conventional methods, is easily implemented with standard microscopy equipment, and is well suited for nanostructures fabricated on planar substrates. The elimination of in-objective illumination in favor of waveguide illumination permits the use of higher numerical-aperture objectives and the collection of higher resolution images. In addition, the evanescent field illumination reduces background scattering and produces higher contrast dark-field images. WSM also provides a consistent illumination geometry across varying instruments, which can eliminate variations in the spectroscopic data collected from similar samples. The waveguide also allows for polarization-controlled illumination using the direction of the incident wavevector, enabling the selective excitation of specific dielectric and metallic scattering resonances. WSM is thus a straightforward and versatile addition to any microscopy apparatus and allows for efficient imaging and spectroscopic analysis of photonic and plasmonic nanostructures.

■ METHODS

Materials. Au nanorods 150 × 50 nm in size were purchased from Nanopartz Inc. (A12-50-700) and used as received. Films of Au nanorods were prepared by functionalizing a substrate with poly-L-lysine (Sigma-Aldrich) and drop casting the Au nanorod solution. Si wafers coated with 100 nm SiO_2 and 200 nm Si_3N_4 (Nova Electronic Materials) were used as opaque substrates for B-DFM and C-WSM. Standard 1 × 3 in. microscopy slides (Fisherbrand 12-550D) and standard microscopy coverslips (Fisherbrand 12-545-M) were used for S-WSM and C-WSM, respectively.

Si NW Growth and Fabrication. Si NWs were grown by the vapor−liquid−solid (VLS) mechanism with a computer-controlled, low-pressure chemical vapor deposition system described previously.[43] To fabricate ENGRAVE structures,[43] NWs were transferred from the growth substrates onto Si wafers and etched by immersing in concentrated buffered hydrofluoric acid (Transense BHF Improved) for 10 s, rinsing in water and 2-propanol, and etching in KOH solution (20.0 g of KOH; 80.0 g of water; 20 mL of 2-propanol as top surface layer) at 40 °C for 40 s.

Sinusoidal NWs. Si NWs were dry transferred from the growth substrate to a Si nitride wafer. The wires were then transferred to a flexible, stretched PDMS substrate (~2 mm thick; Dow Corning Sylgard 184) by direct contact of the two substrates. The tension in the PDMS substrate was slowly released, producing sinusoidal NWs similar to those described in the literature.[47]

Nanohole Fabrication. A Ag film ~170 nm thick was deposited with an electron-beam evaporator (Thermionics VE-100) at normal incidence with a rate of ~1 Å/s at a pressure $<1 \times 10^{-7}$ Torr. Arrays of rectangular nanoholes were fabricated in the Ag film by focused ion beam milling (FEI Helios 600 Nanolab Dual Beam system) at a typical ion acceleration voltage of 30 kV and current of 28 pA. Each nanohole is 200 nm × 260 nm with a pitch of 550 and 450 nm, respectively.

Microscopy. Standard DFM illumination was achieved using white light from a Zeiss HAL 100 halogen lamp installed on a Zeiss AxioImager A2M upright microscope. A 10× objective with a numerical aperture of 0.2 and a working distance of 14.3 mm (Zeiss EC Epiplan 10×/0.2 HD WD = 14.3 M27) was used for low-magnification images and spectra. A 100× objective with a numerical aperture of 0.8 and a working distance of 0.85 mm (Zeiss EC Epiplan 100×/0.8 HD WD = 0.85 M27) was used for high-magnification images and spectra. Waveguide illumination was achieved by coupling a 150 W halogen lamp through a fiber-optic cable (Schott ACE 1) into the end of a glass slide or coverslip. Note that the coupling efficiency into the waveguide is low; nevertheless, the 100−150 W halogen lamps typically installed on commercial microscopes provide sufficient power for WSM. Also note that the exact angle used for coupling the fiber source into the waveguide (see Figure S1) was not observed to have an impact on the images or spectra. All optical images were acquired with a CCD camera (AxioCam ERc 5s). Brightness and contrast adjustment were performed equally on all images. For WSM and DFM images, no corrections for the spectra of the two halogen lamps were applied because of the similarity of the two spectra (see Figure S7). SEM imaging was performed with an FEI Helios 600 Nanolab Dual Beam system with an imaging resolution of <5 nm using a typical acceleration voltage of 5 kV and imaging current of 86 pA.

Scattering Measurements. DFM or WSM images were coupled into a Princeton Instruments Acton SP2500 spectrometer through a fiber-optic cable for spectroscopic analysis. The light was detected by a liquid-nitrogen-cooled CCD array (Princeton Instruments LN/CCD-1340/400) using a 150 groove/mm grating with a blaze angle of 500 nm. Longer wavelengths were collected with a low-pass filter placed in the beam path to prevent detection of second-order diffraction. Background scattering signals were collected in a similar fashion from a region of the sample without nanostructures. The background signal was subtracted from the scattering signal to yield the scattering spectrum. All spectra were divided by the spectrum of the white-light source (see Figure S7) to correct for spectral differences in illumination intensity. The DFM lamp spectrum was obtained using a Labsphere diffuse reflectance standard, and the WSM lamp spectrum was obtained by collecting the light scattered out of the end of the waveguide substrate. All optical measurements were performed after SEM imaging.

Optical Simulations. FDFD finite-element simulations were performed with COMSOL Multiphysics. Three-dimensional optical simulations were implemented using the total-field, scattered-field method. For DFM simulations, the background field was evaluated with a plane wave incident at an oblique angle (~60° with respect to surface normal) on the substrate using periodic boundary conditions on the four horizontal boundaries, a perfectly matched layer (PML) on the lower boundary, and the plane wave source on the upper boundary. The scattered field was then solved after adding the photonic structure to the simulation domain and replacing all boundaries with PMLs. For WSM simulations, a similar approach was utilized, except that the plane wave was incident at an oblique angle (~65° with respect to surface normal) from within the glass substrate to produce total internal reflection in the glass. Images of the surface plasmon modes in Au nanorods were generated by evaluating the scattered electric field intensity ($|E|^2$) in a horizontal plane bisecting the nanorod. Images of the surface plasmon modes in nanohole simulations were produced by evaluating the total field intensity ($|E|^2$) in a horizontal plane 40 nm above the surface of the structure.

■ ASSOCIATED CONTENT

Ⓢ Supporting Information

Supporting Figures S1−S7 showing details of the experimental setup, WSM surface sensitivity, FDFD optical simulations, polarization in the waveguide, coupling mechanism with C-WSM, and halogen lamp spectra. This material is available free of charge via the Internet at http://pubs.acs.org.

■ AUTHOR INFORMATION

Corresponding Author

*E-mail: jfcahoon@unc.edu.

Notes

The authors declare no competing financial interest.

■ ACKNOWLEDGMENTS

This work was wholly supported by the National Science Foundation through grant DMR-1308695. We thank T. Celano for help with figure preparation. We also thank the staff of the Chapel Hill Analytical and Nanofabrication Laboratory (CHANL) user facility for assistance with NW imaging and nanofabrication.

■ REFERENCES

(1) Jain, P. K.; Lee, K. S.; El-Sayed, I. H.; El-Sayed, M. A. Calculated Absorption and Scattering Properties of Gold Nanoparticles of Different Size, Shape, and Composition: Applications in Biological Imaging and Biomedicine. *J. Phys. Chem. B* **2006**, *110*, 7238−7248.

(2) Hu, M.; Novo, C.; Funston, A.; Wang, H.; Staleva, H.; Zou, S.; Mulvaney, P.; Xia, Y.; Hartland, G. V. Dark-Field Microscopy Studies of Single Metal Nanoparticles: Understanding the Factors that Influence the Linewidth of the Localized Surface Plasmon Resonance. *J. Mater. Chem.* **2008**, *18*, 1949−1960.

(3) Kelley, K. L.; Coronado, E.; Zhao, L. L.; Schatz, G. C. The Optical Properties of Metal Nanoparticles: The Influence of Size, Shape, and Dielectric Environment. *J. Phys. Chem. B* **2003**, *107*, 668−677.

(4) Link, S.; El-Sayed, M. A. Shape and Size Dependence of Radiative, Non-Radiative and Photothermal Properties of Gold Nanocrystals. *Int. Rev. Phys. Chem.* **2000**, *19*, 409−453.

(5) Harrick, N. J. *Internal Reflection Spectroscopy*; Interscience Publishers: New York: 1967.

(6) Qi, Z.-m.; Matsuda, N.; Yoshida, T.; Asano, H.; Takatsu, A.; Kato, K. Optical Waveguide Spectrometer Based on Thin-Film Glass Plates. *Opt. Lett.* **2002**, *27*, 2001−2003.

(7) Tcherniak, A.; Ha, J. W.; Dominguez-Medina, S.; Slaughter, L. S.; Link, S. Probing a Century Old Prediction One Plasmonic Particle at a Time. *Nano Lett.* **2010**, *10*, 1398−1404.

(8) Huang, X.; El-Sayed, I. H.; Qian, W.; El-Sayed, M. A. Cancer Cell Imaging and Photothermal Therapy in the Near-Infrared Region by Using Gold Nanorods. *J. Am. Chem. Soc.* **2006**, *128*, 2115−2120.

(9) Murphy, C. J.; Gole, A. G.; Stone, J. W.; Sisco, P. N.; Alkilany, A. M.; Goldsmith, E. C.; Baxter, S. C. Gold Nanoparticles in Biology: Beyond Toxicity to Cellular Imaging. *Acc. Chem. Res.* **2008**, *41*, 1721−1730.

(10) Gao, X.; Yang, L.; Petros, J. A.; Marshall, F. F.; Simons, J. W.; Nie, S. In Vivo Molecular and Cellular Imaging with Quantum Dots. *Curr. Opin. Biotechnol.* **2005**, *16*, 63−72.

(11) Rosi, N. L.; Mirkin, C. A. Nanostructures in Biodiagnostics. *Chem. Rev.* **2005**, *105*, 1547−1562.

(12) Jain, P. K.; Huang, X.; El-Sayed, I. H.; El-Sayed, M. A. Review of Some Interesting Surface Plasmon Resonance-Enhanced Properties of Noble Metal Nanoparticles and Their Applications to Biosystems. *Plasmonics* **2007**, *2*, 107−118.

(13) Schultz, S.; Smith, D. R.; Mock, J. J.; Schultz, D. A. Single-Target Molecule Detection with Nonbleaching Multicolor Optical Immunolabels. *Proc. Natl. Acad. Sci. U.S.A.* **2000**, *97*, 996−1001.

(14) Cao, L.; Fan, P.; Barnard, E. S.; Brown, A. M.; Brongersma, M. L. Tuning the Color of Silicon Nanostructures. *Nano Lett.* **2010**, *10*, 2649−2654.

(15) Brönstrup, G.; Jahr, N.; Leiterer, C.; Csáki, A.; Fritzsche, W.; Christiansen, S. Optical Properties of Individual Silicon Nanowires for Photonic Devices. *ACS Nano* **2010**, *4*, 7113−7122.

(16) Ramos, D.; Gil-Santos, E.; Malvar, O.; Llorens, J. M.; Pini, V.; San Paulo, A.; Calleja, M.; Tamayo, J. Silicon Nanowires: Where Mechanics and Optics Meet at the Nanoscale. *Sci. Rep.* **2013**, *3*, 3445.

(17) Cao, L. Y.; Fan, P. Y.; Brongersma, M. L. Optical Coupling of Deep-Subwavelength Semiconductor Nanowires. *Nano Lett.* **2011**, *11*, 1463−1468.

(18) Willets, K. A.; Van Duyne, R. P. Localized Surface Plasmon Resonance Spectroscopy and Sensing. In *Annual Review of Physical Chemistry*; Annual Reviews: Palo Alto, 2007; Vol. *58*, pp 267−297.

(19) Fan, J. A.; Bao, K.; Lassiter, J. B.; Bao, J.; Halas, N. J.; Nordlander, P.; Capasso, F. Near-Normal Incidence Dark-Field Microscopy: Applications to Nanoplasmonic Spectroscopy. *Nano Lett.* **2012**, *12*, 2817−2821.

(20) Knight, M. W.; Fan, J.; Capasso, F.; Halas, N. J. Influence of Excitation and Collection Geometry on the Dark Field Spectra of Individual Plasmonic Nanostructures. *Opt. Express.* **2010**, *18*, 2579−2587.

(21) Huang, Y.; Kim, D. H. Dark-Field Microscopy Studies of Polarization-Dependent Plasmonic Resonance of Single Gold Nanorods: Rainbow Nanoparticles. *Nanoscale* **2011**, *3*, 3228−3232.

(22) Thoma, F.; Armitage, J.; Trembley, H.; Menges, B.; Langbein, U.; Mittler-Neher, S. Waveguide Scattering Microscopy in Air and Water. In *Opto-Contact: Workshop on Technology Transfers, Start-up Opportunities, and Strategic Alliances*; Corriveau, R. J. L.; Soileau, M. J.; Auger, M., Eds.; SPIE-International Society of Optical Engineering: Bellingham, 1998; Vol. *3414*, pp 242−249.

(23) Thoma, F.; Langbein, U.; Mittler-Neher, S. Waveguide Scattering Microscopy. *Opt. Commun.* **1997**, *134*, 16−20.

(24) Nahar, Q.; Fleißner, F.; Shuster, J.; Morawitz, M.; Halfpap, C.; Stefan, M.; Langbein, U.; Southam, G.; Mittler, S. Waveguide Evanescent Field Scattering Microscopy: Bacterial Biofilms and their Sterilization Response via UV Radiation. *J. Biophotonics* **2013**, Early view DOI:10.1002/jbio.201300135.

(25) Sönnichsen, C.; Geier, S.; Hecker, N. E.; von Plessen, G.; Feldmann, J.; Ditlbacher, H.; Lamprecht, B.; Krenn, J. R.; Aussenegg, F. R.; Chan, V. Z.-H.; et al. Spectroscopy of Single Metallic Nanoparticles Using Total Internal Reflection Microscopy. *Appl. Phys. Lett.* **2000**, *77*, 2949−2951.

(26) Yang, S.-C.; Kobori, H.; He, C.-L.; Lin, M.-H.; Chen, H.-Y.; Li, C.; Kanehara, M.; Teranishi, T.; Gwo, S. Plasmon Hybridization in Individual Gold Nanocrystal Dimers: Direct Observation of Bright and Dark Modes. *Nano Lett.* **2010**, *10*, 632−637.

(27) Koen, K. A.; Weber, M. L.; Mayer, K. M.; Fernandez, E.; Willets, K. A. Spectrally-Resolved Polarization Anisotropy of Single Plasmonic Nanoparticles Excited by Total Internal Reflection. *J. Phys. Chem. C* **2012**, *116*, 16198−16206.

(28) Mock, J. J.; Hill, R. T.; Tsai, Y. J.; Chilkoti, A.; Smith, D. R. Probing Dynamically Tunable Localized Surface Plasmon Resonances of Film-Coupled Nanoparticles by Evanescent Wave Excitation. *Nano Lett.* **2012**, *12*, 1757−1764.

(29) Ha, J. W.; Marchuk, K.; Fang, N. Focused Orientation and Position Imaging (FOPI) of Single Anisotropic Plasmonic Nanoparticles by Total Internal Reflection Scattering Microscopy. *Nano Lett.* **2012**, *12*, 4282−4288.

(30) Marchuk, K.; Fang, N. Three-Dimensional Orientation Determination of Stationary Anisotropic Nanoparticles with Sub-Degree Precision under Total Internal Reflection Scattering Microscopy. *Nano Lett.* **2013**, *13*, 5414−5419.

(31) Axelrod, D. Total Internal Reflection Fluorescence. *Annu. Rev. Biophys. Bioeng.* **1984**, 247−268.

(32) Axelrod, D. Evanescent Excitation and Emission in Fluorescence Microscopy. *Biophys. J.* **2013**, *104*, 1401−1409.

(33) Ni, W.; Chen, H.; Kou, X.; Yeung, M. H.; Wang, J. Optical Fiber-Excited Surface Plasmon Resonance Spectroscopy of Single and Ensemble Gold Nanorods. *J. Phys. Chem. C* **2008**, *112*, 8105−8109.

(34) Chronis, N.; Lee, L. P. Total Internal Reflection-Based Biochip Utilizing a Polymer-Filled Cavity with a Micromirror Sidewall. *Lab Chip* **2004**, *4*, 125−130.

(35) Grandin, H. M.; Stadler, B.; Textor, M.; Voros, J. Waveguide Excitation Fluorescence Microscopy: A New Tool for Sensing and Imaging the Biointerface. *Biosens. Bioelectron.* **2006**, *21*, 1476−1482.

(36) Hassanzadeh, A.; Nitsche, M.; Mittler, S.; Armstrong, S.; Dixon, J.; Langbein, U. Waveguide Evanescent Field Fluorescence Microscopy: Thin Film Fluorescence Intensities and its Application in Cell Biology. *Appl. Phys. Lett.* **2008**, *92*, 233503.

(37) Agnarsson, B.; Ingthorsson, S.; Gudjonsson, T.; Leosson, K. Evanescent-Wave Fluorescence Microscopy Using Symmetric Planar Waveguides. *Opt. Express.* **2009**, *17*, 5075−5082.

(38) Asanov, A.; Zepeda, A.; Vaca, L. A Novel Form of Total Internal Reflection Fluorescence Microscopy (LG-TIRFM) Reveals Different and Independent Lipid Raft Domains in Living Cells. *BBA-Mol. Cell Biol. L.* **2010**, *1801*, 147−155.

(39) Ramachandran, S.; Cohen, D. A.; Quist, A. P.; Lal, R. High Performance, LED Powered, Waveguide Based Total Internal Reflection Microscopy. *Sci. Rep.* **2013**, *3*, 2133.

(40) Sowa, Y.; Steel, B. C.; Berry, R. M. A Simple Backscattering Microscope for Fast Tracking of Biological Molecules. *Rev. Sci. Instrum.* **2010**, *81*, 113704.

(41) Ringe, E.; Sharma, B.; Henry, A. I.; Marks, L. D.; Van Duyne, R. P. Single Nanoparticle Plasmonics. *Phys. Chem. Chem. Phys.* **2013**, *15*, 4110−4129.

(42) Knight, M. W.; Wu, Y.; Lassiter, J. B.; Nordlander, P.; Halas, N. J. Substrates Matter: Influence of an Adjacent Dielectric on an Individual Plasmonic Nanoparticle. *Nano Lett.* **2009**, *9*, 2188−2192.

(43) Christesen, J. D.; Pinion, C. W.; Grumstrup, E. M.; Papanikolas, J. M.; Cahoon, J. F. Synthetically Encoding 10 nm Morphology in Silicon Nanowires. *Nano Lett.* **2013**, *13*, 6281−6286.

(44) Hecht, E. *Optics*, 4th ed.; Addison Wesley: San Francisco, 2002.

(45) Axelrod, D. Total Internal Reflection Fluorescence Microscopy in Cell Biology. *Traffic* **2001**, *2*, 764−774.

(46) Rivas, J.; Muskens, O.; Borgström, M.; Diedenhofen, S.; Bakkers, E. A. M. Optical Anisotropy of Semiconductor Nanowires. In *One-Dimensional Nanostructures*; Wang, Z., Ed.; Springer: New York, 2008; Vol. 3, pp 127−145.

(47) Xu, F.; Lu, W.; Zhu, Y. Controlled 3D Buckling of Silicon Nanowires for Stretchable Electronics. *ACS Nano* **2010**, *5*, 672−678.

(48) Genet, C.; Ebbesen, T. W. Light in Tiny Holes. *Nature* **2007**, *445*, 39−46.

(49) Degiron, A.; Ebbesen, T. W. The Role of Localized Surface Plasmon Modes in the Enhanced Transmission of Periodic Subwavelength Apertures. *J. Opt. A: Pure Appl. Opt.* **2005**, *7*, S90−S96.

(50) van der Molen, K.; Klein Koerkamp, K.; Enoch, S.; Segerink, F.; van Hulst, N.; Kuipers, L. Role of Shape and Localized Resonances in Extraordinary Transmission through Periodic Arrays of Subwavelength Holes: Experiment and Theory. *Phys. Rev. B* **2005**, *72*, 045421.